Kagome Hubbard model from a functional renormalization group perspective

Jonas B. Profe,[1,2,*] Lennart Klebl,[3] Francesco Grandi,[1] Hendrik Hohmann,[4] Matteo Dürrnagel,[4,5] Tilman Schwemmer,[4] Ronny Thomale,[4] and Dante M. Kennes[1,6,†]

[1]*Institut für Theorie der Statistischen Physik, RWTH Aachen University and JARA—Fundamentals of Future Information Technology, 52056 Aachen, Germany*

[2]*Institute for Theoretical Physics, Goethe University Frankfurt, Max-von-Laue-Straße 1, D-60438 Frankfurt a.M., Germany*

[3]*I. Institute for Theoretical Physics, Universität Hamburg, 20148 Hamburg, Germany*

[4]*Institut für Theoretische Physik und Astrophysik and Würzburg-Dresden Cluster of Excellence ct.qmat, Universität Würzburg, 97074 Würzburg, Germany*

[5]*Institute for Theoretical Physics, ETH Zürich, 8093 Zürich, Switzerland*

[6]*Max Planck Institute for the Structure and Dynamics of Matter, Center for Free Electron Laser Science, 22761 Hamburg, Germany*

(Received 21 February 2024; revised 21 May 2024; accepted 31 July 2024; published 30 October 2024)

The recent discovery of a variety of intricate electronic order in kagome metals has sprouted significant theoretical and experimental interest. From an electronic perspective on the potential microscopic origin of these phases, the most basic model is given by a Hubbard model on the kagome lattice. We employ a functional renormalization group (FRG) to analyze the kagome Hubbard model. Through our methodological refinement of FRG both within its N-patch and truncated unity formulation, we resolve previous discrepancies of different FRG approaches [Wang *et al.*, Phys. Rev. B **87**, 115135 (2013) vs Kiesel *et al.*, Phys. Rev. Lett. **110**, 126405 (2013)], and analyze both the pure (p-type) and mixed (m-type) van Hove fillings of the kagome lattice.

DOI: 10.1103/PhysRevResearch.6.043078

I. INTRODUCTION

The vanadium-based kagome metals AV_3Sb_5 (A = K, Cs, Rb) are the most studied class of layered kagome systems so far. A rich interplay between electronic correlations, electron-phonon interactions, geometric frustration and topology is believed to be pivotal in determining their properties [1–4]. At ∼100 K [5], these compounds undergo a charge-order (CO) phase transition leading to a 2×2 in-plane reconstruction of the unit cell. The out-of-plane component of the CO might depend on the cooling rate and on the compound of the series analyzed [6]; it either is $\times 1$ [7], $\times 2$ [8–10] or $\times 4$ [11]. Muon-spin relaxation [12,13], magneto-optical Kerr measurements [14] and polar Kerr results [15] observe a broken time reversal symmetry (TRS) in this phase, with no signatures of magnetic ordering observed. Therefore, this class of kagome metals is a prime contender for realizing the long sought after spontaneous orbital currents reminiscent of the Haldane [16] and the Varma [17] models the latter of which has previously been pursued in high-T_c cuprates [18–20]. Recent high resolution polar Kerr studies, however, do not find any evidence of broken TRS in this state [21].

The controversy of early experimental findings seems to be the rule rather than the exception for this class of compounds. Indeed, several experiments find indications of a phase transition at ∼50 K within the CO domain: Some of them find the transition to a low-temperature nematic phase which might be a zero-momentum charge order [22–24], while others observe a one-dimensional CO with 1×4 in-plane reconstruction [25–27]. Recent investigations do not find any transition around 50 K [28,29], suggesting that the vanadium-based kagome metals might be at the "tipping point" of correlated orders [30], i.e., small perturbations such as strain or an external magnetic field might stabilize a state with *slightly* higher energy than the ground state at pristine conditions.

The properties of the CO state appear to be intertwined with the superconducting phase found below ∼1K, rendering it unconventional in nature. Although a recent experiment points towards conventional s-wave symmetry for the superconducting gap function of the kagome metals [31], several theoretical studies based on the Hubbard model on the kagome lattice have suggested d- [32], $d + id$- [33] and f-wave symmetry [34] for the gap function, which would follow earlier experiments obtaining evidence for an unconventional superconductor [5,35,36]. Furthermore, recent theoretical investigations [37] highlight that the distinction between s and d wave, based on their impurity response, is not as straight forward, hence undermining the argumentation in Ref. [31].

Refined theoretical simulations might help to solve some of the experimental controversies. *Ab initio* descriptions of this class of compounds represent a reasonable starting point to tackle the problem, and they can provide indications on

*Contact author: jonas.hauck@rwth-aachen.de
†Contact author: dante.kennes@mpsd.mpg.de

the minimal models required to describe the salient properties of kagome metals [38,39]. Even if density functional theory seems unable to distinguish the driving force for the CO, which might be electronic or phononic [40–43], still it can provide important indications regarding the Fermiology of the compounds. In particular, two different kinds of van Hove singularities (VHS) [44] are found in the proximity of the Fermi level, suggesting their relevant role for the stabilization of symmetry-broken phases [45]. Despite the fact that more than one orbital per site might be required [46] and electron-phonon interaction might play an important role [47–50] to properly describe the kagome metals, many of the theoretical works consider the single orbital extended Hubbard model to describe the main physical properties of this class of materials. This assumption is based, *inter alia*, on the correct replication of the experimentally observed VHS and their distinct sublattice character, *i.e.,* pure (p-type) and mixed (m-type) sublattice occupation. Further, even though both kinds of VHS are close to the Fermi level in the real systems, several works considered just the p-type VHS, sometimes even neglecting the sublattice character of the states at the Fermi level [51–55], but the role of the m-type VHS has been taken into account in more recent investigations [56–60]. In this work, we clarify the functional renormalization group (FRG) phase diagram of the single orbital extended Hubbard model on the kagome lattice, confirming earlier singular mode FRG (SMFRG) results [32]. Given the relevance of both p- and m-type VHS for the physics of the kagome metals, we study the model at both fillings. We derive an analytical condition for the absence of TRS breaking *at* the phase transition, in agreement with results based on point-group symmetry arguments derived for Ginzburg-Landau theories at a continuous phase transition [61].

The paper is structured as follows. In Secs. II and III we introduce the employed model and give a short introduction to the methods used to examine this model (FRG), respectively. This is followed by Sec. IV where we discuss the phase diagram predicted by truncated unity FRG (TUFRG) and relate it to prior results [32,34]. In Sec. IV A we proceed by an in depth analysis of three different phases found at the p-type VHS, providing an analytic argument to explain providing an analytical argument establishing why a TRS broken charge order is expected to be unstable in a FRG scheme. We then recalculate the phase diagrams with N-patch FRG in Sec. V, highlighting that the two methods yield compatible results when using a state-of-the-art implementation [62]. In Sec. VI we conclude by summarizing the paper and giving an outlook on possible next steps.

II. MODEL

The simplest model possibly describing the rich orderings observed in the AV_3Sb_5 group of kagome metals is the kagome-Hubbard model. We visualize the lattice and Hamiltonian terms in Fig. 1(d). The Hamiltonian is given as

$$H = t \sum_{\langle i,j\rangle,\sigma} c^{\dagger}_{i,\sigma} c_{j,\sigma} + U \sum_{i,} n_{i,\uparrow} n_{i,\downarrow} + V \sum_{\langle i,j\rangle,\sigma\sigma'} n_{i,\sigma} n_{j,\sigma'}, \tag{1}$$

with $c^{(\dagger)}_{i,\sigma}$ the fermionic annihilation/creation operator acting on site i and spin σ, t the nearest neighbor hopping amplitude which we chose as $t = 1$ and measure all energies in units of t from now on. U and V are the on-site and nearest neighbor density-density interactions and $n_{i,\sigma} = c^{\dagger}_{i,\sigma} c_{i,\sigma}$ is the electron density operator on site i and spin σ.

In analog to experimental observations, two dissimilar VHS placed at the M points appear in the band structure, see Figs. 1(a) and 1(c). The difference between the VHS is related to the presence of three sites in the unit cell in the kagome lattice, i.e., three distinct sublattices A, B, and C. When the hopping integral $t > 0$, the upper (lower) VHS is called p-type (m-type) because the Fermi surface at that filling is sublattice *pure* (*mixed*). This means that the Fermi surface has a single (mixed) sublattice character at each M point, which prevents (favors) a nesting condition driven by the local Hubbard interaction, the so-called sublattice interference mechanism [39,63].

III. METHODS

In this work, we apply two different flavors of FRG [64,65], truncated unity FRG [66,67] and N-patch FRG [68]. FRG is based on integrating flow equations starting from a solvable theory to the full solution of the problem. These equations are derived by introducing a cutoff function $R(\Lambda)$ in the single-particle propagator. At the starting point $\Lambda = \Lambda_0$ (here $\Lambda_0 = \infty$), the action is rendered solvable. From this starting point, we successively integrate out the hierarchy of flow equations until the cutoff is removed, thus resulting in the exact solution. For general models, we have to solve an infinite set of coupled differential equations. As a consequence we have to employ approximations that make the equations numerically tractable. In this paper, we utilize the sharp cutoff $R(\Lambda) = \Theta(|\Lambda| - \nu)$ allowing for an efficient implementation of the numerically most demanding parts of the flow. This choice of cutoff limits ourselves to zero temperature, with the flowing cutoff scale taking the role of the Matsubara frequency in the noninteracting Greens function. Thereby the critical temperature is related to the critical scale.

Due to the truncation of the hierarchy, the flow has to be stopped once a coupling becomes too large; if this divergence happens in a nonpolynomial fashion, it signalizes a divergence of a susceptibility and thereby a phase transition. By analyzing the interaction at the divergence, we extract the leading order parameter and predict the expected ordered phase. Here the channels signalize different orderings, each associated with a different fermionic bilinear. The particle-particle channel (P) is associated to Cooper-pair bilinears, its divergence signalizes a superconducting transition. The crossed particle-hole channel (C) is proportional to a spin-operator bilinear, thus resulting in a magnetic order parameter. Lastly, the direct-particle hole channel (D) is proportional to a particle-number operator bilinear, indicating charge ordering, once the magnetic contribution is subtracted.

The two types of FRG we consider in the following are both built upon a level-2 truncated formulation of FRG (vertex-flow FRG), i.e., we discard self-energy feedback and frequency dependences, but keep the

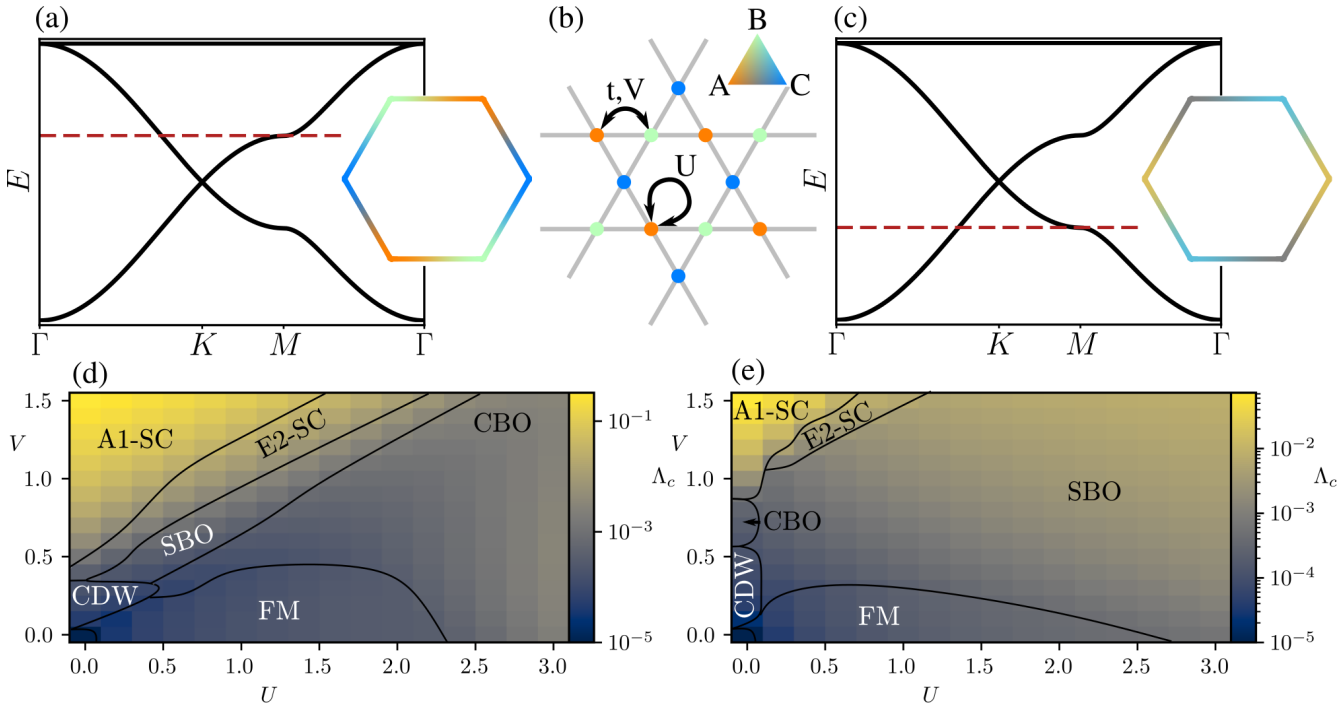

FIG. 1. Band structure, orbital makeup of the FS states at the p and m-type VHS and schematic phase diagrams of the p and m-type filled kagome-Hubbard model. (a) visualizes the band structure with the p-VHS filling marked in red (dashed line). The right panel in subfigure (a) depicts the orbital makeup at the Fermi level, with the colors encoding the admixture of the different sublattices according to (b), that contains the lattice structure with all relevant parameters from the Hamiltonian. (c) is the same as (a) but for the m-type VHS. (d) shows the phase diagram in U-V space at the p-type VHS. We find a ferromagnetic region (FM), a charge density order (CDW), a charge bond order (CBO), a spin bond order (SBO), an E_2 superconductor (E2-SC), and an A_1 superconductor (A1-SC). The phase diagram at the m-type VHS in Fig (e) features the same phases as observed at p-type VHS.

flow of the one-particle irreducible two-particle interaction $F^{\Lambda}_{o_1,o_2,o_3,o_4}(\boldsymbol{k}_1,\boldsymbol{k}_2;\boldsymbol{k}_3)$, where $\boldsymbol{k}_i$ label momenta and o_i is a site index. Here we already utilized that we have $SU(2)$ invariance in our model [69]. The two-particle interaction vertex F describes any interaction which can take place in between two electrons. All possible interaction processes between two electrons comprised in F can be classified into diagrammatic categories, where Φ^P, Φ^D, Φ^C collects all interactions of particle-particle, direct particle-hole and crossed particle-hole type, respectively. Thereby we arrive at the following set of equations for the three diagrammatic channels Φ^x, $x \in \{P, C, D\}$:

$$\frac{d\Phi^{P,\Lambda}_{o_1,o_2,o_3,o_4}(\boldsymbol{k}_1,\boldsymbol{k}_2;\boldsymbol{k}_3)}{d\Lambda} = -\dot{L}^{\Lambda}_{o_1',o_2',o_3',o_4'}(\boldsymbol{k}',\boldsymbol{k}_1+\boldsymbol{k}_2-\boldsymbol{k}')F^{\Lambda}_{o_1,o_2,o_1',o_2'}(\boldsymbol{k}_1,\boldsymbol{k}_2;\boldsymbol{k}')F^{\Lambda}_{o_3',o_4',o_3,o_4}(\boldsymbol{k}',\boldsymbol{k}_1+\boldsymbol{k}_2-\boldsymbol{k}';\boldsymbol{k}_3), \tag{2}$$

$$\frac{d\Phi^{C,\Lambda}_{o_1,o_2,o_3,o_4}(\boldsymbol{k}_1,\boldsymbol{k}_2;\boldsymbol{k}_3)}{d\Lambda} = -\dot{L}^{\Lambda}_{o_1',o_2',o_3',o_4'}(\boldsymbol{k}',\boldsymbol{k}'+\boldsymbol{k}_2-\boldsymbol{k}_3)F^{\Lambda}_{o_1,o_4',o_4o_1'}(\boldsymbol{k}_1,\boldsymbol{k}'+\boldsymbol{k}_2-\boldsymbol{k}_3;\boldsymbol{k}')F^{\Lambda}_{o_3',o_2,o_3,o_2'}(\boldsymbol{k}',\boldsymbol{k}_2;\boldsymbol{k}_3), \tag{3}$$

$$\begin{aligned}\frac{d\Phi^{D,\Lambda}_{o_1,o_2,o_3,o_4}(\boldsymbol{k}_1,\boldsymbol{k}_2;\boldsymbol{k}_3)}{d\Lambda} = \dot{L}^{\Lambda}_{o_1',o_2',o_3',o_4'}(\boldsymbol{k}',\boldsymbol{k}'+\boldsymbol{k}_3-\boldsymbol{k}_1)\big[&2F^{\Lambda}_{o_1,o_4',o_3,o_1'}(\boldsymbol{k}_1,\boldsymbol{k}'+\boldsymbol{k}_3-\boldsymbol{k}_1;\boldsymbol{k}_3)F^{\Lambda}_{o_3',o_2,o_2',o_4}(\boldsymbol{k}',\boldsymbol{k}_2;\boldsymbol{k}'+\boldsymbol{k}_3-\boldsymbol{k}_1)\\ &- F^{\Lambda}_{o_1,o_4',o_3,o_1'}(\boldsymbol{k}_1,\boldsymbol{k}'+\boldsymbol{k}_3-\boldsymbol{k}_1;\boldsymbol{k}_3)F^{\Lambda}_{o_3',o_2,o_4,o_2'}(\boldsymbol{k}',\boldsymbol{k}_2;\boldsymbol{k}_3)\\ &- F^{\Lambda}_{o_1,o_4',o_1',o_3}(\boldsymbol{k}_1,\boldsymbol{k}'+\boldsymbol{k}_3-\boldsymbol{k}_1;\boldsymbol{k}')F^{\Lambda}_{o_3',o_2,o_2',o_4}(\boldsymbol{k}',\boldsymbol{k}_2;\boldsymbol{k}'+\boldsymbol{k}_3-\boldsymbol{k}_1)\big],\end{aligned} \tag{4}$$

where we defined the noninteracting two-particle propagator as In terms of the bare Greens function G^{Λ} and the single scale Greens function $S = \partial_{\Lambda} G^{\Lambda}$

$$\begin{aligned}\dot{L}^{\Lambda}_{1,2,3,4}(\boldsymbol{k}_1,\boldsymbol{k}_2,\boldsymbol{k}_3,\boldsymbol{k}_4) = \big[&S^{\Lambda}_{1,3}(\boldsymbol{k}_1)\,G^{\Lambda}_{2,4}(\boldsymbol{k}_2)\\ &+ G^{\Lambda}_{1,3}(\boldsymbol{k}_1)\,S^{\Lambda}_{2,4}(\boldsymbol{k}_2)\big]\delta_{\boldsymbol{k}_1,\boldsymbol{k}_3}\delta_{\boldsymbol{k}_2,\boldsymbol{k}_4}\,.\end{aligned} \tag{5}$$

The full two-particle vertex F is then obtained by $F = U + \sum_{x\in\{P,C,D\}} \Phi^x$, where U is the two-particle irreducible interaction, here given by the on-site and nearest-neighbor interactions. Differences between truncated unity FRG and N-patch FRG are detailed in Ref. [70] and Appendix A. The details for all simulations are given in Appendix B. Importantly, the two different variants should give consistent results,

which for the kagome Hubbard model has not been the case [32,34], a conundrum we resolve in this paper.

IV. TUFRG RESULTS

We begin by discussing the phase diagram at the two different van Hove types. The prior discussed change in orbital makeup drastically changes the predicted phase diagram, see Figs. 1(d) and 1(e). In both we find the same phases, distinguished by their linearized gap equation solution whose analytic form is detailed in Appendix E, but their phase space volume is vastly different. We find a doubly degenerate $\boldsymbol{q} = 0$ charge-density wave order at low U and V, which will be discussed in detail in Sec. IV A. For small nearest-neighbor interactions we find a large ferromagnetic region. This phase stems from the divergent density of states, which fuels a divergence of the particle-hole loop at low temperatures. In order to obtain this phase, the model's kinetics have to be finely resolved as otherwise the divergence is smeared out by limited momentum resolution. At large V, we find a superconducting order with A_1 symmetry (an s wave) with uniform orbital weight on the three sublattices. At large V the effective on-site interaction becomes attractive, strongly favoring double occupancy and a pair formation to avoid the penalty of having neighboring electrons. Upon lowering V, we enter the E_2 superconducting state, which is discussed in much detail in Refs. [46,71] and briefly revisited in Sec. IV A. Notably, the on-site component of this order parameter does not need to vanish, as we analytically show in Appdenix C. We find that the order parameter weight is approximately evenly split between on-site and nearest-neighbor bonds. The superconducting phases found agree with prior RPA studies [56]. The phase diagram we predict is in some sense complementary to the one found in variational Monte Carlo studies [47] making comparisons difficult. Furthermore, at the m-type VHS we find good agreement between our $V = 0$ line and the one presented in Ref. [60].

All phases mentioned before are located roughly within the same region of the phase diagram at the m and p type VHS, however the spin bond order and charge bond order are not. We name a phase spin or charge bond order if the leading ordering has nonzero weight on a bond and stems from either a crossed or direct particle-hole contribution. Both orders belong to the A_1 irreducible representation with transfer momentum $\boldsymbol{q} = M$ (inducing a 2×2 enlargement of the unit cell). They consist of on-site and bond components, mixing with different weights at different points in the phase diagram. At the p-type VHS, the charge bond-order makes up the largest portion of the phase diagram, while the spin-bond order (SBO) is driven by increased nearest-neighbor interactions on top of the CBO. In contrast, at the m-type VHS, the SBO makes up most parts of the phase diagram, while the CBO is restricted to a very small region at small U and intermediate V.

It should be noted, that these bond orders always mix with the respective on-site density wave. The ratio between bond and on-site order strongly depends on the chosen U and V. To understand the origin of the phases, we examine the case $V = 0$ and unravel what drives the order, by subsequently turning off channels in the FRG calculation. At the m-type VHS the dominant phase is an M point SBO. The bond order character of the phase is induced by the interplay with the other diagrammatic channels: If we perform a flow for only the C channel, we find an M-point spin-density wave roughly agreeing with the phase space of the spin-bond order. By inclusion of the D channel, the critical scale changes by less than 1% (at $U = 3t$), however now the observed order features bond contributions. This indicates that the spin order is primarily driven by RPA-like diagrams, while the bond weights are generated by the higher harmonics induced from the feedback of the P and D channels. To understand why these higher harmonics are amplified, we need to consider the particle-hole loop at the M point:

$$L^{b_1,b_3}_{o_1,o_3}(M) = \int d\boldsymbol{k}\, e^{-i\boldsymbol{k}(\boldsymbol{B}_1-\boldsymbol{B}_3)}(G_{o_1,o_3}(\boldsymbol{k})G_{o_3+b_3,o_1+b_1}(\boldsymbol{k}-M) + G_{o_1,o_3}(\boldsymbol{k}-M)G_{o_3+b_3,o_1+b_1}(\boldsymbol{k})), \tag{6}$$

which we wrote here in the TU formalism, where b_i is the bond connecting the site o_i with another site o_j via the intra unit cell contribution (written as index on the RHS) and the lattice vector $\boldsymbol{B}_i$, for more details see Appendix A. At low critical scales, the main contribution to the integral stems from the two nested Fermi surfaces (FSs) connected by $\boldsymbol{q} = M$. Since at each point along the FS the weight is distributed between at least two orbitals, we obtain nonzero values for all components containing a suitable orbital combination—including the diagonal component $L^{0,0}_{o_1,o_1}$ and the on-site and bond mixing component $L^{0,b_i}_{o_1,o_1}$. Therefore, if the interaction contains a weak bond-order contribution arising from the inter-channel coupling it will get enhanced by the coupling present in the particle-hole loop.

In contrast, the charge bond order at the p-type VHS lacks a parental RPA-like phase, due to the sublattice interference mechanism preventing such an order [63]. If we only flow in the D channel, we encounter no divergence. If we include the C channel, we encounter a divergence in the C channel at critical scales that are larger by an order of magnitude than for the full FRG flow. Therefore, the P channel is a crucial ingredient in suppressing the ferromagnetic divergence. We can understand this again from the loop above. At the p-type VHS the Green's function has weight on at most two of the three orbitals at each point along the Fermi surface. Most importantly, in the high density regions, its weight is concentrated on a single orbital. This suppresses the on-site form factor components of the loop (but they are not zero). So no RPA-like divergence at the M point exists, since the high density regions mainly drive contributions in nontrivial form-factor sectors. Only once the bond components are generated from the C and P channel, we find the bond ordered phase. Note that this dependency on all channels renders the CBO less stable than the SBO. Further, this exemplifies the necessity of numerical studies beyond RPA approximations.

A. Analysis of orders

In the following we give a detailed analysis of the charge orders as well as the E_2 superconducting order at the p-type VHS.

1. Flowing into the symmetry broken phase

After analyzing the leading instabilities from the TUFRG flow two different routes can be taken to extract more information about the form of the symmetry broken state. On the one hand, the FRG flow can be combined with a mean-field analysis of the effective model after the flow reached the critical scale Λ_c [72,73]. Here, one needs to be careful in the construction of the divergence free part of the interactions. On the other hand, one can include self-energies via their flow equation

$$\frac{d\Sigma^{\Lambda}_{1,3}(\boldsymbol{k})}{d\Lambda} = S^{\Lambda}_{4',2'}(\boldsymbol{k}')F^{\Lambda}_{1,2',3,4'}(\boldsymbol{k},\boldsymbol{k}',\boldsymbol{k}) \,, \tag{7}$$

and allow for broken symmetries by insertion of a symmetry breaking perturbation at the initial scale [74,75]. The inclusion of the self-energy to the FRG equations allows for a gap opening during the flow, which, in the exact case (i.e., without truncation of diagrams), cancels the divergence within the vertex-flow equations, see Appendix A. Thereby, the flow can be continued to the symmetry broken state. With this procedure one faces several challenges. First of all, the standard FRG flow equations are not mean-field exact [75–77]. Only once the Katanin-substitution is introduced, the fulfillment of the Ward identities is restored and the flow equations become mean-field exact [78]. This, however, is an issue, as we strongly rely on the sharp cutoff removing frequency integrals from our flow equations which is not possible anymore in the Katanin flow. We can therefore not assume *a priori* that divergences can be removed by allowing broken symmetries. Past results for 1D models, however, do indicate that flowing into symmetry broken charge orders is possible without the inclusion of the Katanin substitution [74].

Since the FRG flow is formulated in the grand canonical ensemble, enabling self-energy feedback implies a flowing particle number. A solution that is frequently employed in self-consistent methods is to adapt the chemical potential after each flow step in order to force a given filling. In this pseudocanonical picture, a counter term is introduced to the diagonal part of the self-energy, effectively altering the system in each step of the iteration. While there are heuristic arguments why this is valid in self-consistent methods, it is known to break down in FRG away from particle-hole symmetry if the Katanin correction is not included [79]. To circumvent possible issues arising from forcing an electron filling to the FRG flow, we perform a search where we vary the *initial* chemical potential to arrive at the right filling value when the stopping condition is met. In Appendix B 2 a we give a more detailed introduction how the flows into the symmetry broken phase are implemented in practice.

2. Charge orders

a. Charge density wave. We first examine the simplest charge order: A charge density wave (orbital order) at $\boldsymbol{q} = 0$ that occurs for small U and nonzero V. The peculiar nature of the Kagome lattice allows for an on-site eigenvector that is in the E_2 irreducible representation. This order parameter hence acts as a site dependent chemical potential. As the Hamiltonian has to be Hermitian, the two order parameters must not be superimposed in a complex fashion. Since nontrivial superpositions of the two eigenvectors may occur nevertheless, we perform a flow into the charge ordered state and visualize the resulting spectral function in Fig. 2.

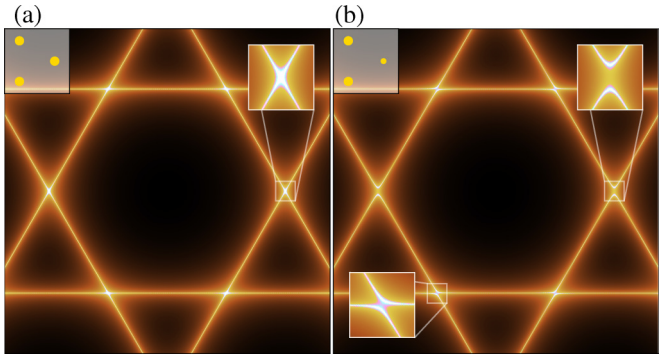

FIG. 2. Spectral function $A(\boldsymbol{k}, \omega = 0)$ for the noninteracting (a) and symmetry broken state (b), respectively. In the upper left panels we visualize the occupation number in the two states on the three different sublattices. From a first FRG run, we found the CDW order to be in the E_2 irreducible representation. The two independent solutions are combined such that all M points are fully gapped.

We observe a transition from a state in which all sites are equally populated to one in which one site is less populated. This charge reordering deforms the Fermi surface to avoid the van Hove singularities at the M-points, which effectively removes the divergence from the FRG flow. The gap-opening breaks the C_{6v} symmetry down to a C_{2v} symmetry, thus we find a Pomeranchuk like instability from electronic repulsion. Notably, if the flow did not open a gap at all VHS, we would expect a divergent susceptibility even in the symmetry broken phase.

b. Charge bond order. In experiments, a time reversal symmetry breaking charge bond order has been observed [12–15]. Since this observation is under current debate, it is desirable to understand whether such a state can be facilitated by purely electronic effects in the single orbital model. To answer this question with FRG, we set up a 2×2 supercell (with 12 sites) that maps the $\boldsymbol{q} = M$ charge order to the Γ point. In this larger system, we repeat the FRG flow with varying random initial symmetry breaking strength, initialized according to the form of the leading eigenvector of the instability in the symmetric phase. An exemplary result of an FRG flow into the symmetry broken phase is visualized in Fig. 3.

In all simulations, we observe a locking between the bond order and on-site components. The preferred configuration features higher occupation on the central hexagons and lower on the tips of the triangles. Furthermore, hopping between sites of the central hexagon is stronger than hopping out of the central hexagon (such a pattern was dubbed anti-tri-hexagonal [55]). The enlarged unit cell leads to the formation of minibands at the M point, see Fig. 3(b). This gapping of the M point again removes the divergence of the susceptibility from the flow allowing us to enter the symmetry broken phase.

As we have a phase locking between charge bond and density order, no time-reversal symmetry breaking can emerge in this state (as otherwise the Hamiltonian becomes non-Hermitian). The locking stems from the particle-hole loop at the M point, see Eq. (6), which enters the linearized (charge

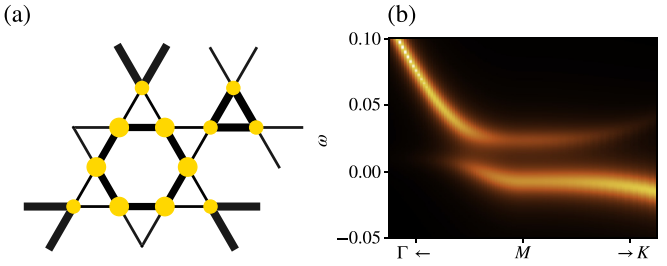

FIG. 3. CBO flow into the symmetry broken phase. On the left we show the predicted charge and hopping modulation in the symmetry broken phase, larger dots/connections indicate higher occupation/hopping. The spectral function around the M point on the right shows the formation of mini-bands at the Fermi level. The slight asymmetry in the minibands stems from the non fixing of the particle number during the FRG flow.

channel) gap equation in the form-factor basis:

$$\lambda \Delta^{b_1}_{o_1} = (2\Phi^D - \Phi^C)^{b_1,b_1'}_{o_1,o_1'} L^{b_1',b_2}_{o_1',o_2} \Delta^{b_2}_{o_2}, \tag{8}$$

where λ is the eigenvalue and Δ is the gap. The physical charge channel is given by $(2\Phi^D - \Phi^C)$ [69]. Here, we immediately observe that if we start with a pure bond order gap, the first matrix multiplication $L^{b_1',b_2}_{o_1',o_2}\Delta^{b_2}_{o_2}$ will result in a gap function mixing on-site and bond components, except if the on-site component is orthogonalized by a suitable imaginary order such as the loop-current order shown in Appendix E. Since such orders can not exploit the weight of the loop in the bond-on-site mixing components mentioned above, they never provide the leading instability and are superseded by real charge orders in the entire phase space. A classification in terms of extended point groups [80] is a natural next step to deepen our understanding of these phases from a group theory perspective. Thus the real bond order instability is a general feature of the spin-1/2 kagome Hubbard model for small gap sizes in the vicinity of the phase transition, assuming a negligible frequency dependence of the charge channel vertex. To find a complex order, we have to remove the on-site components of the interaction decoupling the bond from the density order. The former is for example achieved by considering a spinless model [81]. Alternatively, in more realistic models, this feature can be avoided by the orbital structure of the model under consideration.

B. Superconducting orders

We found that flowing into the superconducting state is not possible without the Katanin substitution as the divergence cannot be removed [76]. Therefore, to analyze the preferred realization of the E_2 superconducting state we have to fall back to conventional methods. To find the energetically favored superposition we extract the gap functions from a linearized gap equation and feed them back into a single step self-consistent mean field equation, allowing us to track the free energy of every initial state, see Fig 4.

We observe minima in the free energy landscape at the $d \pm id$ superposition. Therefore, from this analysis the superconducting order is expected to be chiral [71,82].

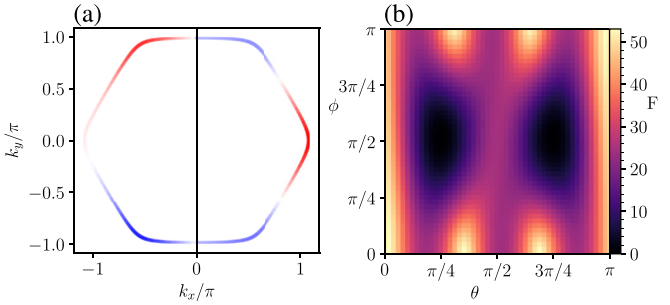

FIG. 4. Chiral superconductivity. In (a) we show the leading eigenvectors from the linearized gap equation, each for one half of the Fermi surface. We find two exactly degenerate eigenfuctions which obey a C_2 symmetry. The gap equation is solved on the Fermi surface. With the obtained linearized gap solutions, we calculate the free energy for different superpositions $\cos(\theta)\psi_1 + \sin(\theta)e^{i\phi}\psi_2$ resulting in (b). We see that chiral superpositions are preferred.

V. N-PATCH RESULTS

N-patch FRG is based on solving the flow equations on the Fermi surface. This is motivated by a power counting argument [64] which shows analytically, that only the contributions of the Fermi surface of the two-particle vertex are not RG irrelevant. In practice, we represent the two-particle interaction as

$$F_{o_1,o_2,o_3,o_4}(\boldsymbol{k}_1, \boldsymbol{k}_2, \boldsymbol{k}_3), \tag{9}$$

where the three momenta are restricted to the Fermi-surface. This however leads to a problem; in general $\boldsymbol{k}_4$ is *not* localized on the Fermi surface. Thereby we implicitly break crossing symmetries, momentum conservation and all point group symmetries. Nonetheless, the application of patching RG has been fruitful [83,84].

To remedy these shortcomings partially, we can perform a resymmetrization of the vertex in each step of the flow. This procedure is well defined on a formal level since, as long as our patches are chosen according to the symmetries, all momenta the vertex explicitly depends on map correctly under symmetries. The fourth momentum enters the symmetry transformation exclusively as a phase prefactor, which we can calculate irrespective of the vertex parametrization:

$$F_{o_1,o_2,o_3,o_4}(\boldsymbol{k}_1, \boldsymbol{k}_2, \boldsymbol{k}_3) = \frac{1}{|\mathcal{G}|} \sum_{S\in\mathcal{G}} S(F_{o_1,o_2,o_3,o_4}(\boldsymbol{k}_1, \boldsymbol{k}_2, \boldsymbol{k}_3)), \tag{10}$$

where S are the symmetry operations contained in the point group of the lattice $\mathcal{G}$. This procedure effectively removes the symmetry breaking and therefore allows us to observe correctly the degeneracies between the eigenvalues in two-dimensional irreducible representations of a point group.

Another subtlety necessitates the flow evaluation in orbital/sublattice space instead of band space. This requirement stems from missing gauge invariance of the two-particle vertex under the orbital to band transformation. In orbital space the matrix element interference is captured better (however still not completely as one finds analogously to Ref. [85]). With these implementational advancements, we calculate the phase diagram, see Fig 5. At the p-type VHS the phase

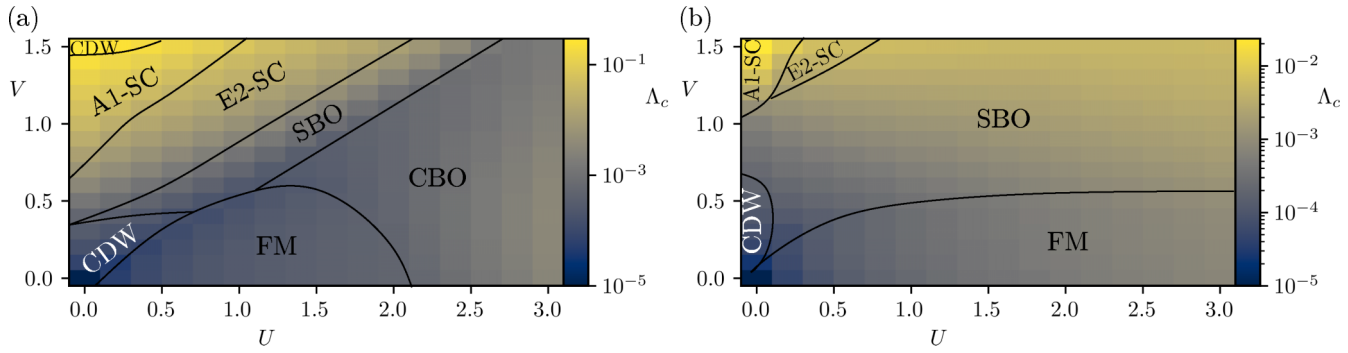

FIG. 5. Schematic phase diagrams of the p- and m-type filled kagome-Hubbard model calculated with N-patch. (a) shows the phase diagram in U-V space at the p-type VHS. We find a ferromagnetic region (FM), a charge density wave (CDW), a charge bond order (CBO), a spin bond order (SBO), an E_2 superconductor (E2-SC) and an A_1 superconductor (A1-SC). (b) shows the phase diagram at the m-type VHS. The same phases as at the p-type VHS are observed, however the CBO is absent.

diagram agrees qualitatively with TUFRG and SMFRG, while at the m-type VHS, we observe two main differences: The ferromagnetic phase is enlarged and the small area of charge bond ordered phase is absent.

As discussed above, the transition from the ferromagnetic to the spin bond order (and its on-site component) is visible in RPA, thus both phases emerge upon the fulfillment of the stoner criterion at either $\boldsymbol{q}_C = 0$ or $\boldsymbol{q}_C = M$. On the RPA level, the transition is observed in N-patch as well, only once the screening from the P-channel is incorporated, the FM is enhanced, while incorporating the D channel leaves the phase diagram invariant. In other words, the feedback from the P- to the C-channel type diagrams strongly suppresses the transition to the antiferromagnet, in contrast to what we observed at the p-type VHS where no such suppression occurred. This fundamental change in behavior can be traced back to the change in orbital content of the Hamiltonian at the M point; while at the p-type VHS we have only weight on a single orbital exactly at the Van Hove points, the weight is split between two orbitals at the m type. This change induces phase slips for the matrix element stemming from the high symmetry points when evaluating one channel at the momentum arguments of another (except when the considered transfer momentum is 0). Therefore, the M point is suppressed by an combination of the mapping back to the FS of the feedback of another channel and the orbital makeup. The D channel does not influence the results as strongly, since its lowest order contribution is U^3 and not U^2 as for the C and P channel. This highlights that for multisite/multiorbital systems a pure N-patch approach is prone to approximation errors at larger scales at which contributions away from the Fermi level are still relevant [85]. A possible remedy is to switch from a truncated unity to an N-patch approach during the flow thereby merging the strengths of each of the methods.

To understand why our N-patch calculation does not agree with the earlier work by Kiesel *et al.* [34], we emphasize the difference in the approach taken. Here we stay in orbital space of the full three-site model, while the work by Kiesel *et al.* works in a projected band space where the effective RG flow was reduced to the van Hove point carrying band. This turns out to be a too drastic approximation for some parts of the phase diagram, in particular when FRG seeks to identify instabilities in the particle-hole channel where the $\log^2$ divergence of the particle-particle channel is only overcome through intermediate coupling strength. With our methodological refinements which avoid the band projection altogether, N-patch FRG works more reliably and matches with the alternative truncated unity formulation.

VI. CONCLUSIONS

We examined the kagome Hubbard model with two different flavors of FRG, N-patch and truncated unity. Our results resolve the tension between earlier FRG results [32,34] by unifying the picture between TUFRG and N-patch highlighting the challenges mutli-orbital models pose in these approaches. Furthermore, we include static self-energy feedback and flow into the symmetry broken phases for both the charge density wave and the charge bond order. Here we found both to be a real superposition of the linearly independent order parameters. The CDW order leads to a deformed Fermi surface which gaps out the Van Hove singularities. This CBO realizes a 2×2 charge order that couples bond with density sectors. Notably, this coupling is a general feature of the single orbital kagome-Hubbard model. This highlights that either the single orbital kagome Hubbard model is not a suitable minimal model for the rich zoo of orderings observed in experiments, or that time reversal symmetry is not broken in the ground state of the system [21,30]. The lack of a flow to a charge ordered state and then to a superconducting phase in our simulations suggests that the single-orbital Hubbard model might not be the proper minimal model to describe the phenomenology of the vanadium-based kagome metals.

In any case, it is of utmost importance to find a valid minimal model describing the physics at play in the kagome metals in order to unravel the puzzling experimental findings. Using models closer to the real materials and linking the FRG flow with *ab initio* simulations [62] seems to be the most promising route.

ACKNOWLEDGMENTS

We thank A. Fischer, M. T. Bunney, F. Ferrari, J. Beyer for fruitful discussions and R. Valenti for carefully reading our

manuscript. This work was supported by the Excellence Initiative of the German federal and state governments, the Ministry of Innovation of North Rhine-Westphalia and the Deutsche Forschungsgemeinschaft (DFG, German Research Foundation). J.B.P., L.K., F.G., D.M.K. acknowledge funding by the DFG under RTG 1995, within the Priority Program SPP 2244 "2DMP"—443274199. L.K. and J.B.P. greatfully acknowledge support from the DFG through FOR 5249 (QUAST, Project No. 449872909, TP5). L.K., J.B.P. and D.M.K. gratefully acknowledge support from the DFG through SPP 2244 (Project No. 422707584). D.M.K. acknowledges support by the Max Planck-New York City Center for Nonequilibrium Quantum Phenomena. We acknowledge computational resources provided through the JARA Vergabegremium on the JARA Partition part of the supercomputer JURECA [86] at Forschungszentrum Jülich. H.H., M.D., T.S., and R.T. received funding from the Deutsche Forschungsgemeinschaft (DFG, German Research Foundation) through Project-ID No. 258499086 - SFB 1170 and through the Würzburg-Dresden Cluster of Excellence on Complexity and Topology in Quantum Matter–*ct.qmat* Project-ID No. 390858490 - EXC 2147.

APPENDIX A: COMPARISON OF TUFRG AND *N*-PATCH

In this section we will first introduce the basic notions and approximations introduced in these two FRG schemes and then compare them. We first begin by the conceptually simpler *N*-patch FRG.

1. N-patch

In *N*-patch FRG we consider the general form of the flow equations [64], without altering them intrinsically. Instead, we reduce the complexity by keeping only very specific momentum components which are chosen to lie on the FS. The motivation for such an approximation is that one can show these components to be the only relevant ones within the two-particle vertex in an RG sense [64] in the limit of low cutoff scales. This greatly reduces the number of points required in the approach, since instead of a two-dimensional (2D) grid, we sample (potential collections) of 1D lines.

This approach is mostly defined in band space and was widely used for single band Hubbard models [84]. The main drawback introduced by the patching approximation stems from restricting the vertex to FS scattering vectors. To be more specific let us consider the flow for the P channel

$$\begin{aligned}\frac{d\Phi^{P,\Lambda}_{1,2,3,4}(\boldsymbol{k}_1,\boldsymbol{k}_2;\boldsymbol{k}_3)}{d\Lambda} &= \frac{1}{2}F^{\Lambda}_{1,2,1',2'}(\boldsymbol{k}_1,\boldsymbol{k}_2;\boldsymbol{k}')F^{\Lambda}_{3',4',3,4}(\boldsymbol{k}',\boldsymbol{k}_1+\boldsymbol{k}_2-\boldsymbol{k}';\boldsymbol{k}_3)\\ &\quad\times \dot{L}^{\Lambda}_{1',2',3',4'}(\boldsymbol{k}',\boldsymbol{k}_1+\boldsymbol{k}_2-\boldsymbol{k}')\,, \end{aligned} \tag{A1}$$

Technically, the summation is performed over the whole Brillouin zone (BZ), the first approximation we have to make is that we can replace it by a summation over the patches. Secondly, even if all momenta refer to patches on the FS, momentum additions, such as $\boldsymbol{k}_1+\boldsymbol{k}_2-\boldsymbol{k}'$, are not necessarily mapping to a $\boldsymbol{k}$ value on the FS. Whenever this is the case, we again have to approximate this momenta by its closest counterpart on the FS. On a fundamental level, since we only know the vertex at the FS, momentum conservation must not necessarily be fulfilled as $\boldsymbol{k}_4=\boldsymbol{k}_1+\boldsymbol{k}_2-\boldsymbol{k}_3$ is not guaranteed to lie on the FS. Thus we break momentum conservation. As a consequence also Grassmann antisymmetry is violated and lattice symmetries are broken. While the latter two can be restored on average, the prior one poses a fundamental problem as the matrix element interference is not fully captured [85], and phase slips due to approximating orbital-to-band transformations by non-matching k points occur when performing calculations in Band space. The second issue is circumvented by performing the *N*-patch calculations in orbital space.

2. TUFRG

While N-patch becomes exact at infinitely small scales, the idea behind TUFRG is to make an expansion of the fermionic momenta in a complete basis and then to truncate this expansion. Since the topic of TUFRG is rather broad we will only summarize the main points important for this manuscript and refer the interested reader to Refs. [66,67,70,87]. We will follow the notation of Ref. [87], technically slightly deviating from standard TUFRG to conserve rotational symmetries with the truncated basis.

First we define the transfer momenta for the different channels as

$$\begin{aligned}\boldsymbol{q}_P &= \boldsymbol{k}_1+\boldsymbol{k}_2=\boldsymbol{k}_4+\boldsymbol{k}_3,\\ \boldsymbol{q}_C &= \boldsymbol{k}_1-\boldsymbol{k}_4=\boldsymbol{k}_3-\boldsymbol{k}_2,\\ \boldsymbol{q}_D &= \boldsymbol{k}_1-\boldsymbol{k}_3=\boldsymbol{k}_4-\boldsymbol{k}_2.\end{aligned} \tag{A2}$$

We define a complete basis mapping a site-orbital index o_x and momentum k to a bond as $g_b(o_x,k)$. To be a complete and orthogonal basis the basis functions have to fulfill

$$\sum_{b_1} g_{b_1}(o_2,k)g^*_{b_1}(o_3,k') = \delta_{k,k'}\delta_{o_2,o_3}, \tag{A3}$$

$$\sum_{o,k} g_{b_1}(o,k)g^*_{b_2}(o,k) = \delta_{b_1,b_2}. \tag{A4}$$

The idea is now that the ladder resummation of a single diagramatic channel results in one bosonic momentum dependence, which we defined above. At low temperatures, the functions usually become rapidly varying with $\boldsymbol{q}$ as one would expect from RPA. On the other hand, the fermionic momenta develop functional dependences much slower and one can therefore expand these in slow varying lattice harmonics [67]. In our case, the basis functions are defined as

$$g_{b_i}(o_j,\boldsymbol{k}) = e^{-i\boldsymbol{k}\boldsymbol{B}_i}\delta_{\boldsymbol{r}_i+\boldsymbol{b}_i,\boldsymbol{r}_j}, \tag{A5}$$

and are truncated according to the real space distance for each site in the lattice individually. We define the Projections onto

the different channels as

$$\hat{P}[F]^{b_1,b_3}_{o_1,o_3}(\boldsymbol{q}_P)^{s_2;s_4}_{s_1;s_3} = \sum_{o_2,o_4,\boldsymbol{k}_1\boldsymbol{k}_3} g_{b_1}(o_2,\boldsymbol{k}_1)g^*_{b_3}(o_4,\boldsymbol{k}_3)F_{o_{1..4}}(\boldsymbol{k}_1,\boldsymbol{q}_P-\boldsymbol{k}_1;\boldsymbol{k}_3)_{s_{1..4}}\ , \tag{A6}$$

$$\hat{C}[F]^{b_1,b_3}_{o_1,o_3}(\boldsymbol{q}_C)^{s_4;s_2}_{s_1;s_3} = \sum_{o_2,o_4,\boldsymbol{k}_1\boldsymbol{k}_3} g_{b_1}(o_4,\boldsymbol{k}_1)g^*_{b_3}(o_2,\boldsymbol{k}_3)F_{o_{1..4}}(\boldsymbol{k}_1,\boldsymbol{k}_1-\boldsymbol{q}_C;\boldsymbol{k}_3)_{s_{1..4}}\ , \tag{A7}$$

$$\hat{D}[F]^{b_1,b_4}_{o_1,o_4}(\boldsymbol{q}_D)^{s_3;s_2}_{s_1;s_4} = \sum_{o_2,o_3,\boldsymbol{k}_1\boldsymbol{k}_4} g_{b_1}(o_3,\boldsymbol{k}_1)g^*_{b_4}(o_2,\boldsymbol{k}_4)F_{o_{1..4}}(\boldsymbol{k}_1,\boldsymbol{k}_4-\boldsymbol{q}_D;\boldsymbol{k}_1-\boldsymbol{q}_D)_{s_{1..4}}\ . \tag{A8}$$

In this new basis the flow equations for a $SU(2)$ symmetric Hamiltonian read

$$\frac{d\hat{P}[\Phi^P]^{b_1,b_3}_{o_1,o_3}(\boldsymbol{q}_P)}{d\Lambda} = -\hat{P}[F]^{b_1,b_1'}_{o_1,o_1'}(\boldsymbol{q}_P)\,L^{pp;b_1',b_3'}_{o_1',o_3'}(\boldsymbol{q}_P)\,\hat{P}[F]^{b_3',b_3}_{o_3',o_3}(\boldsymbol{q}_P), \tag{A9}$$

$$\frac{d\hat{C}[\Phi^C]^{b_1,b_3}_{o_1,o_3}(\boldsymbol{q}_C)}{d\Lambda} = -\hat{C}[F]^{b_1,b_1'}_{o_1,o_1'}(\boldsymbol{q}_C)L^{ph;b_1',b_3'}_{o_1',o_3'}(\boldsymbol{q}_C)\hat{C}[F]^{b_3',b_3}_{o_3',o_3}(\boldsymbol{q}_C)\ , \tag{A10}$$

$$\begin{aligned}\frac{d\hat{D}[\Phi^D]^{b_1,b_4}_{o_1,o_4}(\boldsymbol{q}_D)}{d\Lambda} =& L^{ph;b_1',b_4'}_{o_1',o_4'}(\boldsymbol{q}_D)\big(2\hat{D}[F]^{b_1,b_1'}_{o_1,o_1'}(\boldsymbol{q}_D)\hat{D}[F]^{b_4',b_4}_{o_4',o_4}(\boldsymbol{q}_D) - \hat{C}[F]^{b_1,b_1'}_{o_1,o_1'}(\boldsymbol{q}_D)\hat{D}[F]^{b_4',b_4}_{o_4',o_4}(\boldsymbol{q}_D)\\ &- \hat{D}[F]^{b_1,b_1'}_{o_1,o_1'}(\boldsymbol{q}_D)\hat{C}[F]^{b_4',b_4}_{o_4',o_4}(\boldsymbol{q}_D)\big)\ .\end{aligned} \tag{A11}$$

The two-particle propagator L is in this basis given as (already integrating out the sharp cutoff)

$$\begin{aligned}L^{ph;b_1,b_3}_{o_1,o_3}(\boldsymbol{q}_X) &= \frac{1}{2\pi}\int_{\boldsymbol{k}} e^{-i\boldsymbol{B}_1\boldsymbol{k}}e^{i\boldsymbol{B}_3\boldsymbol{k}}\big(G^{\Lambda}_{o_1;o_3}(\boldsymbol{k})G^{\Lambda}_{o_1+b_1;o_3+b_3}(\boldsymbol{k}-\boldsymbol{q}_X)+G^{-\Lambda}_{o_1;o_3}(\boldsymbol{k})G^{-\Lambda}_{o_1+b_1;o_3+b_3}(\boldsymbol{k}-\boldsymbol{q}_X)\big),\\ L^{pp;b_1,b_3}_{o_1,o_3}(\boldsymbol{q}_P,) &= -\frac{1}{2\pi}\int_{\boldsymbol{k}} e^{-i\boldsymbol{B}_1\boldsymbol{k}}e^{i\boldsymbol{B}_3\boldsymbol{k}}\big(G^{-\Lambda}_{o_1;o_3}(\boldsymbol{k})G^{\Lambda}_{o_1+b_1;o_3+b_3}(\boldsymbol{q}_P-\boldsymbol{k})+G^{\Lambda}_{o_1;o_3}(\boldsymbol{k})G^{-\Lambda}_{o_1+b_1;o_3+b_3}(\boldsymbol{q}_P-\boldsymbol{k})\big)\ .\end{aligned} \tag{A12}$$

In this basis, the self-energy equation reads

$$\begin{aligned}\frac{d\Sigma_{o_1,o_3}(\boldsymbol{k})}{d\Lambda} =& -\frac{1}{2\pi}\sum_{\nu=\pm\Lambda} 2G_{o_2';o_4'}(\boldsymbol{k}',\nu)\\ &\times\big[g^*_{b_1'}(o_2',\boldsymbol{k})g_{b_3'}(o_4',\boldsymbol{k})P^{b_1',b_3'}_{o_1,o_3}(\boldsymbol{k}+\boldsymbol{k}',\nu)\\ &+ g^*_{b_1'}(o_4',\boldsymbol{k})g_{b_3'}(o_2',\boldsymbol{k})C^{b_1',b_3'}_{o_1,o_3}(\boldsymbol{k}-\boldsymbol{k}',-\nu)\\ &+ g^*_{b_1'}(o_3,\boldsymbol{k})g_{b_4'}(o_2',\boldsymbol{k}')D^{b_1,b_4}_{o_1,o_4}(0)\big]\\ &+ \frac{1}{2\pi}\sum_{\nu=\pm\Lambda} G_{o_2';o_4'}(\boldsymbol{k}',\nu)\\ &\times\big[g^*_{b_1'}(o_2',\boldsymbol{k})g_{b_4'}(o_3',\boldsymbol{k}')P^{b_1',b_3'}_{o_1,o_3}(\boldsymbol{k}+\boldsymbol{k}',\nu+)\\ &+ g^*_{b_1'}(o_4',\boldsymbol{k})g_{b_3'}(o_2',\boldsymbol{k})D^{b_1',b_3'}_{o_1,o_3}(\boldsymbol{k}-\boldsymbol{k}',-\nu)\\ &+ g^*_{b_1'}(o_3,\boldsymbol{k})g_{b_4'}(o_2',\boldsymbol{k}')C^{b_1',b_4'}_{o_1,o_4'}(0)\big]\ .\end{aligned} \tag{A13}$$

TUFRG introduces a systematic error as we cut away feedback in between the channels from high harmonics. This feedback is expected to become more important at lower critical scales. Further, we introduce a bias towards low harmonic orders due to the finite harmonic truncation. Therefore, one usually performs convergence checks ensuring that no relevant contributions were neglected.

3. Summary

TUFRG and *N*-patch are technically approximations coming from different regimes of critical scales. While TUFRG is build around the limit of large critical scales and expanded upon a known exact representation there, *N*-patch is build around power counting arguments for very small critical scales. Both methods are technically constructed such that the full solution can be recovered (either by adding more form factors or by adding additional points away from the FS). However, this is unpractical for complex models.

APPENDIX B: NUMERICAL DETAILS

In this subsection we provide the necessary numerical details to reproduce the calculations at hand. For all calculations we used the divERGe library [62] and its predecessor the TU^{2}FRG code.

1. N-patch

For the *N*-patch calculations, we used the autopatching function of divERGe, with 6 patching points within the irreducible Brillouin zone (IBZ) wedge. Thus in total we used 72 points along the FS. For the integration of the flow equations, we used the diverge Euler integrator with its default parameters, except increasing the initial Λ value to 100. We checked that resymmetrizing the vertex during the flow does not influence that phase we diverge into, but merely ensures that E_2 eigenvalues are approximately degenerate. The bare two-particle propagator is calculated on a 2000^2 grid for the *p*-type and on a 2400^2 grid for the *m*-type calculation. The flow equations are averaged over the Graßmann antisymmetry related contributions to ensure that the vertices obey these on average. This requires us to explicitly store the loop for three momenta $\boldsymbol{q}, \boldsymbol{k}, \boldsymbol{k}'$ and sum over equivalent parametrizations of the diagrams.

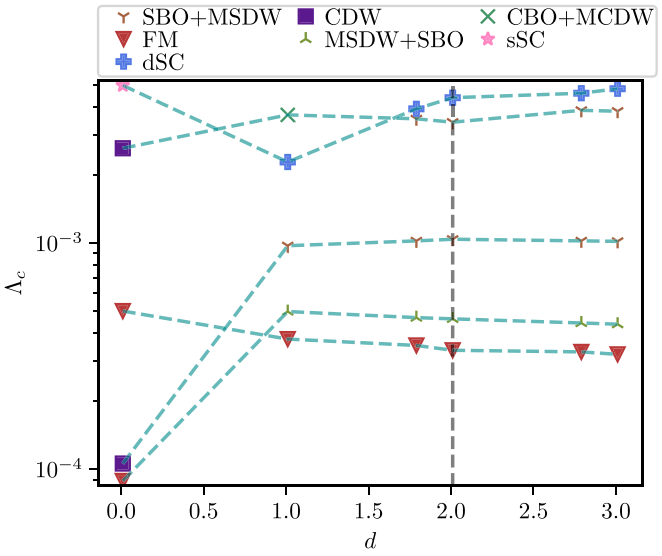

FIG. 6. Phases and critical scales at various points in the phase diagram as a function of bond distance d. The chosen bond distance is depicted as a grey dashed line. We find that the found phases are stable for the chosen cutoff, while the exact critical scale changes on a quantitative level.

2. TUFRG

For the TUFRG calculation of the phase diagram, we employed a 36×36 mesh for the bosonic momenta in each of the channels. For the loop we utilized an additional refinement of 45×45. The integration of the flow equations is performed with a Bogacki-Shampine integrator allowing for an relative error of 10^{-2} and an absolute error of 10^{-3}. For each site, we include all bonds with a real-space length shorter than $2.01d$, which we checked to be sufficient for obtaining convergent phases, see Fig 6.

Flowing into the ordered state

For flowing to the ordered state, we first pick the unit cell, matching the expected ordering, for the CDW this is the standard unit cell, while for the CBO this is a 2×2 unit cell with 12 sites, which in turn results in a backfolded BZ. Then we add a random initial symmetry breaking, which is ensured to be Hermitian and run the FRG flow for a set of these random initialization. We control the maximal amplitude of the randomness as a convergence parameter, which should be smaller than the expected critical scale we aim to reach such that it cannot have any influence to the expected ordering. Additionally we track the grand-canonical potential by including its flow equation which reads [88]

$$\partial_\Lambda \Omega_\Lambda = \frac{1}{2\pi} \sum_{\omega=\pm\Lambda} \mathrm{Tr}[1 - G_0(i\omega)\Sigma(i\omega)] \,. \tag{B1}$$

Further, we perform flows at fixed and non-fixed particle number. Thus in total we track the static self-energy, the static vertex and the grand canonical potential during the flow. In practice we include the static contribution of both the self-energy and the vertex during the flow and solve the coupled set of differential equations, keeping the momentum dependence of both. Notably, in our case, the divergence in the vertex is indeed suppressed by the gap opening in the self-energy, which is not necessarily the case in the used truncation scheme. For charge orders this was found to be true in Ref. [74]. The calculations with self-energy feedback are performed on a 48×48 mesh for the $\boldsymbol{q}$ dependence of the vertices, with an additional refinement of 15×15 for the loop. To obtain the self-energy on the fine grid, we perform a Fourier interpolation.

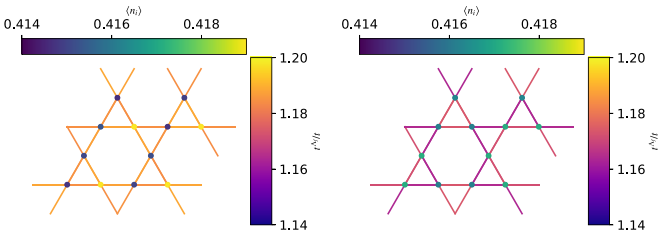

FIG. 7. Two solutions of the flow equations at fixed particle number. The left forms a C_2 breaking DW order, while the right forms a anti-tri-hexagonal order. The DW order is slightly higher in energy and cannot be recovered in flows without fixing the particle number.

First, let us discuss the CBO flows. For the flows at non-fixed particle number, the initial filling required such that the flow terminates at the van Hove filling of the bare system is about $0.33x$ slightly dependent on the initial symmetry breaking. As expected, we find that a symmetry breaking of $\approx 10^{-5}$ does not influence the outcome of the calculation anymore. When fixing the filling, we are able to stabilize two different orderings (depending on the random seed). We find the one presented in the main text and, –at slightly higher energy, a C_2 breaking CDW order, see Fig 7. The preferred solution should, from the energetic viewpoint, be the one presented in the main text. To verify that this is not an artifact of fixing the particle number we repeat the calculation without fixed particle number. We adapt the initial filling such that at the end we are at the van Hove filling of the noninteracting system. In agreement with what was predicted by the energetics arguments, we only find the solution presented in the main text. Since in both schemes, this solution is the preferred one, we conclude that this is the order FRG predicts.

We follow the same procedure for the CDW order, for which we do not find competing solutions from the fixed particle number flows or the nonfixed particle number flows.

APPENDIX C: S WAVE IN E2

In the triangular and honeycomb lattice it is common knowledge that the E_2 irreducible representation does not allow for an on-site component of the order parameter. This follows directly from the requirement that the mirror planes have character 0. In the kagome lattice we will prove in the following that this is not true, by explicitly constructing the system of equations and solving it. We label the three sites a, b, and c and the corresponding complex numbers α, β, and γ. To calculate the character we have to apply the point group symmetry and calculate $\chi = \sum_i \boldsymbol{v}_i^* \mathbf{O} \boldsymbol{v}_i$ where i runs over the subspace dimension ($v_0 = \boldsymbol{v}$, $v_1 = \boldsymbol{w}$). We will focus on the on-site component of the ordering vector, restricting $\boldsymbol{v}$ and $\boldsymbol{w}$ to three component vectors. For the mirror planes we have

$\chi = 0$. The mirrors exchange two sites, while the third maps onto itself. The C_6 rotation maps $a \to c, c \to b, b \to a$, The C_3 rotation maps $a \to b, b \to c, c \to a$. We directly observe that their inverse operations behave identically to the other rotation therefore the rotations give us instead of four conditions only two. The C_2 maps every site onto itself, and thus acts as an identity. We will assume normalized three component vectors, thus the E/C_2 condition is trivially fulfilled. An additional requirement is that the two vectors have to span a 2D space. The resulting set of equations read:

$$\begin{aligned}
0 &= v_a^* v_a + v_b^* v_c + v_c^* v_b + w_a^* w_a + w_b^* w_c + w_c^* w_b,\\
0 &= v_b^* v_b + v_a^* v_c + v_c^* v_a + w_b^* w_b + w_a^* w_c + w_c^* w_a,\\
0 &= v_c^* v_c + v_b^* v_a + v_a^* v_b + w_c^* w_c + w_b^* w_a + w_a^* w_b,\\
-1 &= v_a^* v_b + v_b^* v_c + v_c^* v_a + w_a^* w_b + w_b^* w_c + w_c^* w_a,\\
-1 &= v_a^* v_c + v_c^* v_b + v_b^* v_a + w_a^* w_c + w_c^* w_b + w_b^* w_a,\\
0 &= v_a^* w_a + v_b^* w_b + v_c^* w_c.
\end{aligned}$$

The equations are solved by $v_a = 0, v_b = 1/\sqrt{2}\cdot\phi, v_c = -v_b, w_a = -2w_b, w_b = 1/\sqrt{6}\cdot\gamma, w_c = w_b$, where ϕ and γ are global phases. As can be seen by insertion

$$\begin{aligned}
2|v_b|^2 &= 6|w_b|^2,\\
|v_b|^2 &= 3|w_b|^2,\\
|v_b|^2 &= 3|w_b|^2,\\
-1 &= -|v_b|^2 + -3|w_b|^2,\\
-1 &= -|v_b|^2 + -3|w_b|^2,\\
0 &= v_b^* w_b - v_b^* w_b.
\end{aligned}$$

The phases of $\boldsymbol{v}$ and $\boldsymbol{w}$ are free parameters. Since we found the on-site components of the order parameter vector we initially started to fulfill all restrictions due to symmetry, we found the specific form of the on-site component of the E_2 irrep.

APPENDIX D: EXISTENCE OF A FERROMAGNETIC STATE

In the following we will argue that the weak interaction ferromagnet, which was not seen in some recent studies, has to be present in the thermodynamic limit. Since we are interested in the weak-coupling limit, RPA arguments will suffice. In general we can rewrite the particle-hole loop at zero momentum transfer as

$$\begin{aligned}
[b]L(0) &= \sum_{\omega,k} G(\omega,k)G(\omega,k)\\
&= \sum_k n_f(\epsilon(k))(1-n_f(\epsilon(k)))\\
&= \int d\epsilon\, \rho(\epsilon) n_f(\epsilon)(1-n_f(\epsilon)),
\end{aligned} \tag{D1}$$

where $\rho(\epsilon)$ is the density of states and $n_f(\epsilon)$ is the Fermi distribution. For a more general multiband model we need to project this loop onto the eigenvector corresponding to a FM, which has equal weight on all sites within the unit cell (we sum out all doubly occurring indices)

$$\begin{aligned}
v_i L_{ij} v_j &= v_i G(\omega,k)_{ij} G(\omega,k)_{ji} v_j\\
&= [t]\frac{1}{3}\sum_{k,\alpha,\beta} \frac{1}{i\omega - \epsilon(k,\alpha)} \frac{1}{i\omega - \epsilon(k,\beta)}\\
&\quad \times \sum_i U_{i,\alpha}(k) U_{i,\beta}(k)^* \sum_j U_{j,\beta}(k) U_{j,\alpha}(k)^*\\
&= \frac{1}{3}\sum_{k,\alpha} \frac{1}{i\omega - \epsilon(k,\alpha)} \frac{1}{i\omega - \epsilon(k,\alpha)}\\
&= -\frac{1}{3T}\sum_{k,\alpha} n_f(\epsilon(k,\alpha))[1 - n_f(\epsilon(k,\alpha))],
\end{aligned} \tag{D2}$$

where $\epsilon(k,\alpha)$ is the dispersion of band α at momentum k given as

$$\begin{aligned}
\epsilon(k,1) &= 2t,\\
\epsilon(k,2/3) &= t(-1 \pm \sqrt{4A(k) - 3})\\
\text{with } A(k) &= \cos^2\left(\frac{k\cdot R_1}{2}\right) + \cos^2\left(\frac{k\cdot R_2}{2}\right)\\
&\quad + \cos^2\left(\frac{k\cdot(R_2 - R_1)}{2}\right)
\end{aligned}$$

with R_1 and R_2 being the basis vectors of the kagome lattice. At the p-type VHS the flat band plays no role. Furthermore we can restrict the summation to an irreducible BZ wedge in which only one band crosses the Fermi level, here we pick for simplicity one in which band 2 crosses. Thus we obtain

$$v_i L_{ij} v_j = -\frac{4}{T}\sum_k n_f(\epsilon(k,2))(1 - n_f(\epsilon(k,2))). \tag{D3}$$

We can now rewrite this in terms of the density of states of the band as in Eq. (6):

$$v_i L_{ij} v_j = -\frac{4}{3T}\int d\epsilon\, \rho(\epsilon) n_f(\epsilon)(1 - n_f(\epsilon)). \tag{D4}$$

We have $n_f(\epsilon)(1 - n_f(\epsilon)) = \delta_T(\epsilon)$ where $\delta_T(\epsilon)$ is a smeared out Dirac delta distribution, thus we get

$$v_i L_{ij} v_j \approx -\frac{4}{T}\rho(0). \tag{D5}$$

Since we are at the van Hove singularity, the density of states is logarithmically diverging. This divergence is cut off by finite size effects explaining its absence in some earlier studies [47]. In the TDL the ferromagnetic phase should be existent as long as no other phase gaps out the system beforehand.

APPENDIX E: ORDER PARAMETERS OF THE FOUND PHASES

In the following, we will detail the general analytical form of the linearized gap equation solutions for the orders we found in our FRG simulations, see Fig. 1, in site + position space, thus the fermionic arguments are encoded in the site indices and the bosonic argument is encoded in the dependence on the unit-cell distance $\boldsymbol{R}$. Further we highlight how these change between p-type and m-type van Hove singularities.

FM. The ferromagnetic phase is a $\boldsymbol{q} = 0$ phase ($\boldsymbol{R}$ independent) and orbitally nonselective it belongs to the A_1 irreducible representation of the C_{6v} group and the order parameter mathematically reads

$$\Delta_{i,j}(\boldsymbol{R})^{FM} = \delta_{i,j}\Delta_0\ (1,1,1)_i^T, \tag{E1}$$

where Δ_0 is the real valued amplitude of the phase. *CDW.* At both, the $m-$ and p-type van-Hove dopings, the CDW belongs to the E_2 irreducible representation, is peaked at $\boldsymbol{q} = 0$ and is orbitally selective. Due to the E_2 nature of the order the gap functions are only specifically picked representatives and different vectors can be achieved by recombination of these (this is also the case for all other E_2 orders). The order has the form

$$\Delta_{i,j}(\boldsymbol{R})^{\mathrm{CDW},1} = \delta_{i,j}\Delta_0\ (0,1,-1)_i^T, \tag{E2}$$

$$\Delta_{i,j}(\boldsymbol{R})^{\mathrm{CDW},2} = \delta_{i,j}\Delta_0\ (1,0,-1)_i^T. \tag{E3}$$

The combination realizing the minimal energy is visualized in Fig. 2.

A_1-SC. As the ferromagnet, the A_1-SC belongs to the A_1 irreducible representation of the C_{6v} group, is orbitally non selective and is peaked at $\boldsymbol{q} = 0$. The corresponding energy gap is given by

$$\Delta_{i,j}(\boldsymbol{R})^{A_1} = \delta_{i,j}\Delta_0\ (1,1,1)_i^T, \tag{E4}$$

which is identical to the FM phase (note that the corresponding electronic operator pair is a different one).

E_2-SC. A in detail analysis of the E_2 superconducting order has been given in Ref. [71]. It is a $\boldsymbol{q} = 0$ order with both on-site and higher form-factor components belonging to the E_2 irreducible representation of C_{6v}. The exact weight distribution between on-site, nearest- and second- nearest neighbor depends on the point in the phase diagram, resulting in a rather complicated linearized gap form. In general, the order parameter can be classified according to its weight on the different distance shells

$$\Delta_{o_1,o_2}(\boldsymbol{R})^{E_2,i} = \big(\delta_{o_1,o_2}\Delta_0^i + \delta_{\langle o_1,o_2\rangle}\Delta_1^i + \delta_{\langle\langle o_1,o_2\rangle\rangle}\Delta_2^i + ...\big), \tag{E5}$$

while on each distance shell we have two gap functions transforming according to the E_2 irreducible representation. The different distance shells do couple thus the gaps on different distances are not independent.

CBO/CDW. The CBO/CDW phase is a $\boldsymbol{q} = M$ phase and has a three component order parameter. The general form of its gap function reads

$$\Delta_{o_1,o_2}(\boldsymbol{R})^{\mathrm{CBO},i} = e^{i\boldsymbol{R}\boldsymbol{M}_i}\big(\delta_{o_1,o_2}\Delta^i_{0;o_1} + \delta_{\langle o_1,o_2\rangle}\Delta^i_{1;o_1,o_2} + \delta_{\langle\langle o_1,o_2\rangle\rangle}\Delta^i_{2;o_1,o_2} + ...\big). \tag{E6}$$

In the case examined in the main text, the higher distance gaps are strongly suppressed, thus only the first two orders remain, with $(\Delta_1^i)_{o_1,o_2} = A$ for connections between A and B/C sublattice and $-A$ for the connection between B and C sublattices. The phase alternates this pattern between neighboring unit cells.

SBO/SDW. The SBO/SDW phase is, as the CBO/CDW, a $\boldsymbol{q} = M$ phase and it has a three component order parameter. Within a linearized gap approximation, the gap functions of these two are only differing by their spin dependence (here we picked an S^z representation)

$$\Delta_{o_1,o_2}(\boldsymbol{R})^{\mathrm{SBO},i,s} = \sigma^z_{s,s}e^{i\boldsymbol{R}\boldsymbol{M}_i}\big(\delta_{o_1,o_2}\Delta^i_{0;o_1} + \delta_{\langle o_1,o_2\rangle}\Delta^i_{1;o_1,o_2} + \delta_{\langle\langle o_1,o_2\rangle\rangle}\Delta^i_{2;o_1,o_2} + ...\big), \tag{E7}$$

LCO. Our FRG calculations are also capturing imaginary charge orderlike loop current orders, that attracted enormous attention in the literature. In our calculations, however, the LCO is subleading for all parameter settings. For completeness we show such a subleading solution and give the form of the order parameter. Its general order parameter is of the form

$$\Delta_{o_1,o_2}(\boldsymbol{R})^{\mathrm{LCO},i} = ie^{i\boldsymbol{R}\boldsymbol{M}_i}\tilde{\Delta}_{o_1,o_2}(\boldsymbol{R}), \tag{E8}$$

where $\tilde{\Delta}_{o_1,o_2}(\boldsymbol{R}) = -\tilde{\Delta}_{o_2,o_1}(-\boldsymbol{R})$, thus by definition the LCO is not allowed to have an on-site component. Below, we show one such LCO solution found subleading but stable in the postflow linerized gap equation, which is stable under the linearized gap equation is visualized in Fig. 8.

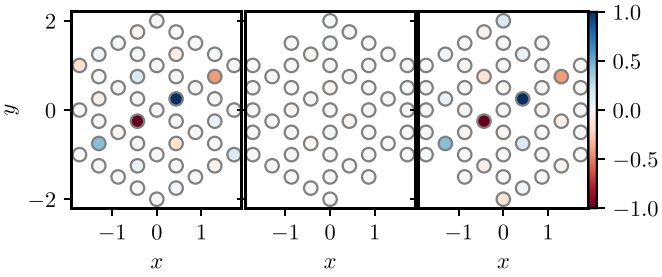

FIG. 8. Loop current order Δ_{o_1,o_2} at a single M-point transfer momentum from the linearized charge-sector gap equation for the three sublattices o_1 (left to right) normalized such that the largest component is 1.

[1] T. Neupert, M. M. Denner, J.-X. Yin, R. Thomale, and M. Z. Hasan, Charge order and superconductivity in kagome materials, Nat. Phys. **18**, 137 (2022).

[2] K. Jiang, T. Wu, J.-X. Yin, Z. Wang, M. Z. Hasan, S. D. Wilson, X. Chen, and J. Hu, Kagome superconductors AV_3Sb_5 (A = K, Rb, Cs), Natl. Sci. Rev. **10**, nwac199 (2023).

[3] Z. Guguchia, R. Khasanov, and H. Luetkens, Unconventional charge order and superconductivity in kagome-lattice systems as seen by muon-spin rotation, npj Quantum Mater. **8**, 41 (2023).

[4] Y. Hu, X. Wu, A. P. Schnyder, and M. Shi, Electronic landscape of kagome superconductors AV_3Sb_5 (A = K, Rb, Cs) from angle-resolved photoemission spectroscopy, npj Quantum Mater. **8**, 67 (2023).

[5] B. R. Ortiz, S. M. L. Teicher, Y. Hu, J. L. Zuo, P. M. Sarte, E. C. Schueller, A. M. M. Abeykoon, M. J. Krogstad, S. Rosenkranz,

R. Osborn, R. Seshadri, L. Balents, J. He, and S. D. Wilson, CsV_3Sb_5: A $\mathbb{Z}_2$ topological kagome metal with a superconducting ground state, Phys. Rev. Lett. **125**, 247002 (2020).

[6] Q. Xiao, Y. Lin, Q. Li, X. Zheng, S. Francoual, C. Plueckthun, W. Xia, Q. Qiu, S. Zhang, Y. Guo, J. Feng, and Y. Peng, Coexistence of multiple stacking charge density waves in kagome superconductor CsV_3Sb_5, Phys. Rev. Res. **5**, L012032 (2023).

[7] H. Li, G. Fabbris, A. H. Said, J. P. Sun, Y.-X. Jiang, J.-X. Yin, Y.-Y. Pai, S. Yoon, A. R. Lupini, C. S. Nelson, Q. W. Yin, C. S. Gong, Z. J. Tu, H. C. Lei, J.-G. Cheng, M. Z. Hasan, Z. Wang, B. Yan, R. Thomale, H. N. Lee, and H. Miao, Discovery of conjoined charge density waves in the kagome superconductor CsV_3Sb_5, Nat. Commun. **13**, 6348 (2022).

[8] Y.-X. Jiang, J.-X. Yin, M. M. Denner, N. Shumiya, B. R. Ortiz, G. Xu, Z. Guguchia, J. He, M. S. Hossain, X. Liu, J. Ruff, L. Kautzsch, S. S. Zhang, G. Chang, I. Belopolski, Q. Zhang, T. A. Cochran, D. Multer, M. Litskevich, Z.-J. Cheng, X. P. Yang, Z. Wang, R. Thomale, T. Neupert, S. D. Wilson, and M. Z. Hasan, Unconventional chiral charge order in kagome superconductor KV_3Sb_5, Nat. Mater. **20**, 1353 (2021).

[9] H. Li, T. T. Zhang, T. Yilmaz, Y. Y. Pai, C. E. Marvinney, A. Said, Q. W. Yin, C. S. Gong, Z. J. Tu, E. Vescovo, C. S. Nelson, R. G. Moore, S. Murakami, H. C. Lei, H. N. Lee, B. J. Lawrie, and H. Miao, Observation of unconventional charge density wWave without acoustic phonon anomaly in kagome superconductors AV_3Sb_5 (A = Rb, Cs), Phys. Rev. X **11**, 031050 (2021).

[10] Z. Liang, X. Hou, F. Zhang, W. Ma, P. Wu, Z. Zhang, F. Yu, J.-J. Ying, K. Jiang, L. Shan, Z. Wang, and X.-H. Chen, Three-dimensional charge density wave and surface-dependent vortex-core states in a kagome superconductor CsV_3Sb_5, Phys. Rev. X **11**, 031026 (2021).

[11] B. R. Ortiz, S. M. L. Teicher, L. Kautzsch, P. M. Sarte, N. Ratcliff, J. Harter, J. P. C. Ruff, R. Seshadri, and S. D. Wilson, Fermi surface mapping and the nature of charge-density-wave order in the kagome superconductor CsV_3Sb_5, Phys. Rev. X **11**, 041030 (2021).

[12] C. Mielke III, D. Das, J.-X. Yin, H. Liu, R. Gupta, Y.-X. Jiang, M. Medarde, X. Wu, H. C. Lei, J. Chang, P. Dai, Q. Si, H. Miao, R. Thomale, T. Neupert, Y. Shi, R. Khasanov, M. Z. Hasan, H. Luetkens, and Z. Guguchia, Time-reversal symmetry-breaking charge order in a kagome superconductor, Nature (London) **602**, 245 (2022).

[13] R. Khasanov, D. Das, R. Gupta, C. Mielke, M. Elender, Q. Yin, Z. Tu, C. Gong, H. Lei, E. T. Ritz, R. M. Fernandes, T. Birol, Z. Guguchia, and H. Luetkens, Time-reversal symmetry broken by charge order in CsV_3Sb_5, Phys. Rev. Res. **4**, 023244 (2022).

[14] Y. Xu, Z. Ni, Y. Liu, B. R. Ortiz, Q. Deng, S. D. Wilson, B. Yan, L. Balents, and L. Wu, Three-state nematicity and magneto-optical Kerr effect in the charge density waves in kagome superconductors, Nat. Phys. **18**, 1470 (2022).

[15] Y. Hu, S. Yamane, G. Mattoni, K. Yada, K. Obata, Y. Li, Y. Yao, Z. Wang, J. Wang, C. Farhang, J. Xia, Y. Maeno, and S. Yonezawa, Time-reversal symmetry breaking in charge density wave of CsV_3Sb_5 detected by polar Kerr effect, arXiv:2208.08036.

[16] F. D. M. Haldane, Model for a quantum Hall effect without Landau levels: Condensed-matter realization of the "parity anomaly", Phys. Rev. Lett. **61**, 2015 (1988).

[17] C. M. Varma, Non-Fermi-liquid states and pairing instability of a general model of copper oxide metals, Phys. Rev. B **55**, 14554 (1997).

[18] P. Bourges, D. Bounoua, and Y. Sidis, Loop currents in quantum matter, Comptes Rendus. Phys. **22**, 7 (2021).

[19] M. Greiter and R. Thomale, No evidence for spontaneous orbital currents in numerical studies of three-band models for the CuO planes of high temperature superconductors, Phys. Rev. Lett. **99**, 027005 (2007).

[20] R. Thomale and M. Greiter, Numerical analysis of three-band models for CuO planes as candidates for a spontaneous T-violating orbital current phase, Phys. Rev. B **77**, 094511 (2008).

[21] D. R. Saykin, C. Farhang, E. D. Kountz, D. Chen, B. R. Ortiz, C. Shekhar, C. Felser, S. D. Wilson, R. Thomale, J. Xia, and A. Kapitulnik, High resolution polar Kerr effect studies of CsV_3Sb_5: Tests for time-reversal symmetry breaking below the charge-order transition, Phys. Rev. Lett. **131**, 016901 (2023).

[22] L. Nie, K. Sun, W. Ma, D. Song, L. Zheng, Z. Liang, P. Wu, F. Yu, J. Li, M. Shan, D. Zhao, S. Li, B. Kang, Z. Wu, Y. Zhou, K. Liu, Z. Xiang, J. Ying, Z. Wang, T. Wu, and X. Chen, Charge-density-wave-driven electronic nematicity in a kagome superconductor, Nature (London) **604**, 59 (2022).

[23] L. Zheng, Z. Wu, Y. Yang, L. Nie, M. Shan, K. Sun, D. Song, F. Yu, J. Li, D. Zhao, S. Li, B. Kang, Y. Zhou, K. Liu, Z. Xiang, J. Ying, Z. Wang, T. Wu, and X. Chen, Emergent charge order in pressurized kagome superconductor CsV_3Sb_5, Nature (London) **611**, 682 (2022).

[24] D. Wulferding, S. Lee, Y. Choi, Q. Yin, Z. Tu, C. Gong, H. Lei, S. Yousuf, J. Song, H. Lee, T. Park, and K.-Y. Choi, Emergent nematicity and intrinsic versus extrinsic electronic scattering processes in the kagome metal CsV_3Sb_5, Phys. Rev. Res. **4**, 023215 (2022).

[25] H. Zhao, H. Li, B. R. Ortiz, S. M. L. Teicher, T. Park, M. Ye, Z. Wang, L. Balents, S. D. Wilson, and I. Zeljkovic, Cascade of correlated electron states in the kagome superconductor CsV_3Sb_5, Nature (London) **599**, 216 (2021).

[26] H. Li, S. Wan, H. Li, Q. Li, Q. Gu, H. Yang, Y. Li, Z. Wang, Y. Yao, and H.-H. Wen, No observation of chiral flux current in the topological kagome metal CsV_3Sb_5, Phys. Rev. B **105**, 045102 (2022).

[27] H. Li, D. Oh, M. Kang, H. Zhao, B. R. Ortiz, Y. Oey, S. Fang, Z. Ren, C. Jozwiak, A. Bostwick, E. Rotenberg, J. G. Checkelsky, Z. Wang, S. D. Wilson, R. Comin, and I. Zeljkovic, Small Fermi pockets intertwined with charge stripes and pair density wave order in a kagome superconductor, Phys. Rev. X **13**, 031030 (2023).

[28] Z. Liu, Y. Shi, Q. Jiang, E. W. Rosenberg, J. M. DeStefano, J. Liu, C. Hu, Y. Zhao, Z. Wang, Y. Yao, D. Graf, P. Dai, J. Yang, X. Xu, and J.-H. Chu, Absence of nematic instability in the kagome metal CsV_3Sb_5, Phys. Rev. X **14**, 031015 (2024).

[29] M. Frachet, L. Wang, W. Xia, Y. Guo, M. He, N. Maraytta, R. Heid, A.-A. Haghighirad, M. Merz, C. Meingast, and F. Hardy, Colossal c-axis response and lack of rotational symmetry breaking within the kagome plane of the CsV_3Sb_5 superconductor, arXiv:2310.06102.

[30] C. Guo, G. Wagner, C. Putzke, D. Chen, K. Wang, L. Zhang, M. Gutierrez-Amigo, I. Errea, M. G. Vergniory, C. Felser, M. H. Fischer, T. Neupert, and P. J. W. Moll, Correlated order at the tipping point in the kagome metal CsV_3Sb_5, Nat. Phys. **20**, 579 (2024).

[31] W. Zhang, X. Liu, L. Wang, C. W. Tsang, Z. Wang, S. T. Lam, W. Wang, J. Xie, X. Zhou, Y. Zhao, S. Wang, J. Tallon, K. T. Lai, and S. K. Goh, Nodeless superconductivity in kagome metal CsV_3Sb_5 with and without time reversal symmetry breaking, Nano Lett. **23**, 872 (2023).

[32] W.-S. Wang, Z.-Z. Li, Y.-Y. Xiang, and Q.-H. Wang, Competing electronic orders on kagome lattices at van Hove filling, Phys. Rev. B **87**, 115135 (2013).

[33] S.-L. Yu and J.-X. Li, Chiral superconducting phase and chiral spin-density-wave phase in a Hubbard model on the kagome lattice, Phys. Rev. B **85**, 144402 (2012).

[34] M. L. Kiesel, C. Platt, and R. Thomale, Unconventional Fermi surface instabilities in the kagome Hubbard model, Phys. Rev. Lett. **110**, 126405 (2013).

[35] Q. Yin, Z. Tu, C. Gong, Y. Fu, S. Yan, and H. Lei, Superconductivity and normal-state properties of kagome metal RbV_3Sb_5 single crystals, Chin. Phys. Lett. **38**, 037403 (2021).

[36] Z. Guguchia, C. Mielke, D. Das, R. Gupta, J.-X. Yin, H. Liu, Q. Yin, M. H. Christensen, Z. Tu, C. Gong, N. Shumiya, M. S. Hossain, T. Gamsakhurdashvili, M. Elender, P. Dai, A. Amato, Y. Shi, H. C. Lei, R. M. Fernandes, M. Z. Hasan, H. Luetkens, and R. Khasanov, Tunable unconventional kagome superconductivity in charge ordered RbV_3Sb_5 and KV_3Sb_5, Nat. Commun. **14**, 153 (2023).

[37] S. C. Holbæk, M. H. Christensen, A. Kreisel, and B. M. Andersen, Unconventional superconductivity protected from disorder on the kagome lattice, Phys. Rev. B **108**, 144508 (2023).

[38] M. Fuchs, P. Liu, T. Schwemmer, G. Sangiovanni, R. Thomale, C. Franchini, and D. Di Sante, Kagome metal-organic frameworks as a platform for strongly correlated electrons, J. Phys.: Materials **3**, 025001 (2020).

[39] A. Consiglio, T. Schwemmer, X. Wu, W. Hanke, T. Neupert, R. Thomale, G. Sangiovanni, and D. Di Sante, Van Hove tuning of AV_3Sb_5 kagome metals under pressure and strain, Phys. Rev. B **105**, 165146 (2022).

[40] X. Zhou, Y. Li, X. Fan, J. Hao, Y. Dai, Z. Wang, Y. Yao, and H.-H. Wen, Origin of charge density wave in the kagome metal CsV_3Sb_5 as revealed by optical spectroscopy, Phys. Rev. B **104**, L041101 (2021).

[41] C. Wang, S. Liu, H. Jeon, Y. Jia, and J.-H. Cho, Charge density wave and superconductivity in the kagome metal CsV_3Sb_5 around a pressure-induced quantum critical point, Phys. Rev. Mater. **6**, 094801 (2022).

[42] C. Wang, S. Liu, H. Jeon, and J.-H. Cho, Origin of charge density wave in the layered kagome metal CsV_3Sb_5, Phys. Rev. B **105**, 045135 (2022).

[43] A. Ptok, A. Kobiałka, M. Sternik, J. Łażewski, P. T. Jochym, A. M. Oleś, and P. Piekarz, Dynamical study of the origin of the charge density wave in AV_3Sb_5 ($A =$ K, Rb, Cs) compounds, Phys. Rev. B **105**, 235134 (2022).

[44] L. Van Hove, The occurrence of singularities in the elastic frequency distribution of a crystal, Phys. Rev. **89**, 1189 (1953).

[45] Y. Hu, X. Wu, B. R. Ortiz, S. Ju, X. Han, J. Ma, N. C. Plumb, M. Radovic, R. Thomale, S. D. Wilson, A. P. Schnyder, and M. Shi, Rich nature of Van Hove singularities in kagome superconductor CsV_3Sb_5, Nat. Commun. **13**, 2220 (2022).

[46] X. Wu, T. Schwemmer, T. Müller, A. Consiglio, G. Sangiovanni, D. Di Sante, Y. Iqbal, W. Hanke, A. P. Schnyder, M. M. Denner, M. H. Fischer, T. Neupert, and R. Thomale, Nature of unconventional pairing in the kagome superconductors AV_3Sb_5 ($A =$ K, Rb, Cs), Phys. Rev. Lett. **127**, 177001 (2021).

[47] F. Ferrari, F. Becca, and R. Valentí, Charge density waves in kagome-lattice extended Hubbard models at the van Hove filling, Phys. Rev. B **106**, L081107 (2022).

[48] M. Kang, S. Fang, J. Yoo, B. R. Ortiz, Y. M. Oey, J. Choi, S. H. Ryu, J. Kim, C. Jozwiak, A. Bostwick, E. Rotenberg, E. Kaxiras, J. G. Checkelsky, S. D. Wilson, J.-H. Park, and R. Comin, Charge order landscape and competition with superconductivity in kagome metals, Nat. Mater. **22**, 186 (2022).

[49] D. Subires, A. Korshunov, A. H. Said, L. Sánchez, B. R. Ortiz, S. D. Wilson, A. Bosak, and S. Blanco-Canosa, Order-disorder charge density wave instability in the kagome metal $(Cs,Rb)V_3Sb_5$, Nat. Commun. **14**, 1015 (2023).

[50] Q.-G. Yang, M. Yao, D. Wang, and Q.-H. Wang, Charge bond order and *s*-wave superconductivity in the kagome lattice with electron-phonon coupling and electron-electron interaction, Phys. Rev. B **109**, 075130 (2024).

[51] M. M. Denner, R. Thomale, and T. Neupert, Analysis of charge order in the kagome metal AV_3Sb_5 ($A =$ K, Rb, Cs), Phys. Rev. Lett. **127**, 217601 (2021).

[52] T. Park, M. Ye, and L. Balents, Electronic instabilities of kagome metals: Saddle points and Landau theory, Phys. Rev. B **104**, 035142 (2021).

[53] Y.-P. Lin and R. M. Nandkishore, Complex charge density waves at Van Hove singularity on hexagonal lattices: Haldane-model phase diagram and potential realization in the kagome metals AV_3Sb_5 ($A =$ K, Rb, Cs), Phys. Rev. B **104**, 045122 (2021).

[54] J.-W. Dong, Z. Wang, and S. Zhou, Loop-current charge density wave driven by long-range Coulomb repulsion on the Kagomé lattice, Phys. Rev. B **107**, 045127 (2023).

[55] F. Grandi, A. Consiglio, M. A. Sentef, R. Thomale, and D. M. Kennes, Theory of nematic charge orders in kagome metals, Phys. Rev. B **107**, 155131 (2023).

[56] A. T. Rømer, S. Bhattacharyya, R. Valentí, M. H. Christensen, and B. M. Andersen, Superconductivity from repulsive interactions on the kagome lattice, Phys. Rev. B **106**, 174514 (2022).

[57] H. D. Scammell, J. Ingham, T. Li, and O. P. Sushkov, Chiral excitonic order from twofold van Hove singularities in kagome metals, Nat. Commun. **14**, 605 (2023).

[58] X. Wu, D. Chakraborty, A. P. Schnyder, and A. Greco, Crossover between electron-electron and electron-phonon mediated pairing on the kagome lattice, Phys. Rev. B **109**, 014517 (2024).

[59] J. Huang, R. Tazai, Y. Yamakawa, S. Onari, and H. Kontani, Low temperature phase transitions inside the CDW phase in the kagome metals AV_3Sb_5($A =$ Cs, Rb, K): Significance of mixed-type Fermi surface electron correlations, Phys. Rev. B **109**, L041110 (2024).

[60] Y.-Q. Liu, Y.-B. Liu, W.-S. Wang, D. Wang, and Q.-H. Wang, Electronic orders on the kagome lattice at the lower van Hove filling, Phys. Rev. B **109**, 075127 (2024).

[61] J. L. Birman, Simplified theory of symmetry change in second-order phase transitions: Application to V_3Si, Phys. Rev. Lett. **17**, 1216 (1966).

[62] J. Profe, D. Kennes, and L. Klebl, diverge implements various exact renormalization group examples, SciPost Phys. Codebases 26 (2024).

[63] M. L. Kiesel and R. Thomale, Sublattice interference in the kagome Hubbard model, Phys. Rev. B **86**, 121105(R) (2012).

[64] W. Metzner, M. Salmhofer, C. Honerkamp, V. Meden, and K. Schonhammer, Functional renormalization group approach to correlated fermion systems, Rev. Mod. Phys. **84**, 299 (2012).

[65] N. Dupuis, L. Canet, A. Eichhorn, W. Metzner, J. Pawlowski, M. Tissier, and N. Wschebor, The nonperturbative functional renormalization group and its applications, Phys. Rep. **910**, 1 (2021).

[66] C. Husemann and M. Salmhofer, Efficient parametrization of the vertex function, Ω scheme, and the t, t' Hubbard model at van Hove filling, Phys. Rev. B **79**, 195125 (2009).

[67] J. Lichtenstein, D. S. d. l. Peña, D. Rohe, E. D. Napoli, C. Honerkamp, and S. A. Maier, High-performance functional renormalization group calculations for interacting fermions, Comput. Phys. Commun. **213**, 100 (2017).

[68] C. Honerkamp, M. Salmhofer, N. Furukawa, and T. M. Rice, Breakdown of the Landau-Fermi liquid in two dimensions due to umklapp scattering, Phys. Rev. B **63**, 035109 (2001).

[69] M. Salmhofer and C. Honerkamp, Fermionic renormalization group flows: Technique and theory, Prog. Theor. Phys. **105**, 1 (2001).

[70] J. Beyer, J. B. Hauck, and L. Klebl, Reference results for the momentum space functional renormalization group, Eur. Phys. J. B **95**, 65 (2022).

[71] T. Schwemmer, H. Hohmann, M. Dürrnagel, J. Potten, J. Beyer, S. Rachel, Y.-M. Wu, S. Raghu, T. Müller, W. Hanke, and R. Thomale, Sublattice modulated superconductivity in the kagome Hubbard model, Phys. Rev. B **110**, 024501 (2024).

[72] J. Reiss, D. Rohe, and W. Metzner, Renormalized mean-field analysis of antiferromagnetism and d-wave superconductivity in the two-dimensional Hubbard model, Phys. Rev. B **75**, 075110 (2007).

[73] S.-J. O, Consistent combination of truncated-unity functional renormalization group and mean-field theory, Phys. Rev. B **109**, 205118 (2024).

[74] L. Markhof, B. Sbierski, V. Meden, and C. Karrasch, Detecting phases in one-dimensional many-fermion systems with the functional renormalization group, Phys. Rev. B **97**, 235126 (2018).

[75] R. Gersch, J. Reiss, and C. Honerkamp, Fermionic functional renormalization-group for first-order phase transitions: A mean-field model, New J. Phys. **8**, 320 (2006).

[76] M. Salmhofer, C. Honerkamp, W. Metzner, and O. Lauscher, Renormalization group flows into phases with broken symmetry, Prog. Theor. Phys. **112**, 943 (2004).

[77] R. Gersch, C. Honerkamp, D. Rohe, and W. Metzner, Fermionic renormalization group flow into phases with broken discrete symmetry: Charge-density wave mean-field model, Eur. Phys. J. B **48**, 349 (2005).

[78] A. A. Katanin, Fulfillment of Ward identities in the functional renormalization group approach, Phys. Rev. B **70**, 115109 (2004).

[79] D. Rohe, Quasi-particle functional renormalisation group calculations in the two-dimensional t-t′-Hubbard model, SciPost Phys. **15**, 192 (2023).

[80] J. W. F. Venderbos, Symmetry analysis of translational symmetry broken density waves: Application to hexagonal lattices in two dimensions, Phys. Rev. B **93**, 115107 (2016).

[81] J. Zhan, H. Hohmann, M. Dürrnagel, R. Fu, S. Zhou, Z. Wang, R. Thomale, X. Wu, and J. Hu, Loop current order on the kagome lattice (unpublished).

[82] R. Nandkishore, L. S. Levitov, and A. V. Chubukov, Chiral superconductivity from repulsive interactions in doped graphene, Nat. Phys. **8**, 158 (2012).

[83] M. L. Kiesel, C. Platt, W. Hanke, D. A. Abanin, and R. Thomale, Competing many-body instabilities and unconventional superconductivity in graphene, Phys. Rev. B **86**, 020507(R) (2012).

[84] C. Honerkamp and M. Salmhofer, Temperature-flow renormalization group and the competition between superconductivity and ferromagnetism, Phys. Rev. B **64**, 184516 (2001).

[85] L.-H. Chen, Z. Liu, and J.-T. Zheng, Matrix element interference in N-patch functional renormalization group, Phys. Rev. B **99**, 085119 (2019).

[86] P. Thörnig, JURECA: Data centric and booster modules implementing the modular supercomputing architecture at Jülich supercomputing centre, JLSRF **7**, A182 (2021).

[87] J. B. Hauck and D. M. Kennes, TU^{2}FRG: A scalable approach for truncated unity functional renormalization group in generic fermionic models, Eur. Phys. J. B **95**, 60 (2022).

[88] C. Karrasch, The functional renormalization group for zero-dimensional quantum systems in and out of equilibrium, Ph.D. thesis, Aachen, 2010.